Journal of Materials Research and Technology 28 (2024) 1875–1882

Contents lists available at ScienceDirect

Journal of Materials Research and Technology

journal homepage: www.elsevier.com/locate/jmrt

Cost-effective synthesis of copper sulfide nanoparticles and flexible films for photocatalytic and antibiotic applications

Jina Jung [a], Hye Jin Jeon [b], Sung Woong Yang [a], Myeong-geun Choi [a], Devthade Vidyasagar [a], Jeong Hyeok Kim [a], Ryun Bo Shim [a], Yeonghun Yun [e], Sehoon Han [f], In Sun Cho [c,d,**], Jee Eun Han [b,***], Sangwook Lee [a,*]

[a] School of Materials Science and Engineering, Kyungpook National University, Daegu, 41566, Republic of Korea
[b] College of Veterinary Medicine, Kyungpook National University, Daegu 41566, Republic of Korea
[c] Department of Materials Science & Engineering, Ajou University, Suwon 16499, Republic of Korea
[d] Department of Energy Systems Research, Ajou University, Suwon 16499, Republic of Korea
[e] Department Perovskite Tandem Solar Cells, Helmholtz-Zentrum Berlin für Materialien und Energie GmbH, 12489, Berlin, Germany
[f] ShareChem, Daejeon, 34121, Republic of Korea

ARTICLE INFO

Handling editor:P.Y. Chen

Keywords:
Copper sulfide
Scalable synthesis
Nanoflowers
Photocatalyst
Antibiotic film

ABSTRACT

Herein, we investigate the effects of temperature and thiourea addition rate on the synthesis of copper sulfide nanoparticles (CuS NPs) via a chemical co-precipitation method, exploring their impact on the size and morphology of CuS NPs. Our systematic approach resulted in the successful synthesis of CuS NPs with significantly smaller nanoflower sizes than previously reported in the literature, providing insights into the nucleation and growth mechanisms under various synthesis conditions. Furthermore, the photocatalytic activity of the synthesized CuS NPs with three types of distinctive morphologies, namely, nanoflowers with 50 nm diameter (F-50), nanoflowers with 200 nm diameter, and nanogravels with 50 nm diameter, is comparatively analyzed. Notably, the F-50 exhibits a superior photocatalytic performance compared to the other samples, demonstrating the considerable influence of the NP size and morphology on their functional properties. Furthermore, the antibacterial property of the small CuS nanoflowers is examined using an antibacterial film fabricated by coating the NPs on a polyethylene terephthalate substrate, which is widely used as a protective or packaging film in various industries because of its transparency and flexibility. The antibacterial film can be used to kill both gram-positive and -negative bacteria effectively. This research contributes significantly to the understanding and optimization of CuS NP synthesis and application, emphasizing the potential of small-sized nanoflower CuS NPs in photocatalysis and antibacterial applications.

1. Introduction

The emergence of several new antibiotic-resistant bacteria threatens the existence of various creatures and adversely affects human health. These bacteria live and multiply on most surfaces, including human skin, floors, devices, and packages. Researchers have been exploring various materials and approaches to produce a universal antimicrobial agent with broad bactericidal activity and applicability. Metals, oxides, and sulfides, including Au, Ag, Cu, Pt, Pd, ZnO, TiO_2, and CuS, have been studied as antimicrobial agents [1–8]. These antimicrobial agents produce reactive oxygen species (ROS) that damages cell membranes and eventually kill bacteria [9]. Among these agents, copper has been widely used for commercial applications, as it is an earth-abundant element and is less expensive than other novel metals. However, it poses a significant toxicity risk to humans and is susceptible to oxidation when exposed to ambient atmosphere [10]. In contrast, copper sulfide (CuS) has higher biocompatibility and chemical stability compared to copper metal and possesses superior antimicrobial activity [11]. The high stability of CuS enables its effective stabilization and application in the form of nanoparticles (NPs), leading to excellent antibacterial

* Corresponding author.
** Corresponding author. Department of Materials Science & Engineering, Ajou University, Suwon 16499, Republic of Korea.
*** Corresponding author.
E-mail addresses: insuncho@ajou.ac.kr (I.S. Cho), jehan@knu.ac.kr (J.E. Han), wook2@knu.ac.kr (S. Lee).

https://doi.org/10.1016/j.jmrt.2023.12.100
Received 13 October 2023; Received in revised form 1 December 2023; Accepted 11 December 2023
Available online 15 December 2023

activity owing to unique features comprising small sizes, high surface-to-volume ratios, and diverse morphologies [12].

Previous studies have demonstrated the synthesis of CuS NPs with various morphologies, such as nanoflowers [13], nonoplates [14,15], hollow spheres [16,17], nanowires [18,19], and nanocubes [20]. Among these morphologies, nanoflowers assembled with nanoplates have shown exceptional photocatalytic and antibacterial performances due to their abundant active sites and efficient light absorption [21–24]. Mutalik et al. demonstrated that CuS nanoflowers exhibited enhanced ROS production, both in the presence and absence of light irradiation, compared to microspheres and nanoparticles [8]. Adhikari et al. reported that CuS nanoflowers exhibited the highest photocatalytic activity among various morphologies, such as nanoflowers, nanoplates, and nanowires [22]. Zhang et al. reported that nanoflowers exhibited higher photocatalytic activity than doughnut-shaped dense nanospheres, attributed to the enhanced light absorption resulting from the cavity-mirror effect, inducing multiple light scatterings within the nanoflower [23]. Based on these preceding studies, the morphology, specifically the shape and size, of CuS NPs emerges as a critical factor influencing their photocatalytic and antimicrobial activities.

However, synthesizing tiny flower-shaped NPs is challenging because the nucleus should be formed rapidly and simultaneously, and further growth should be suppressed to obtain small NPs. Additionally, to obtain nanoflower morphology, the nuclei should be grown further to form nanoplates with a preferential orientation, followed by self-assembly [25,26]. Therefore, carefully controlling the nucleation and growth during the synthesis process is essential to obtain nanoflowers. Although many articles have been published on morphology control, only a few reports are available on controlling the size of the nanoflowers. Furthermore, most nanoflowers reported thus far have micron-sized particles [13,24,27,28], with the smallest particle diameter being 100 nm [29].

In this study, we successfully synthesized flower-shaped CuS NPs with a particle diameter of 50 nm via a cost-effective and scalable chemical co-precipitation method. Furthermore, the nucleation and growth mechanisms are discussed depending on the temperature and thiourea addition rate. Among the synthesized CuS NPs with various morphologies, such as small nanoflowers with 50 nm diameter (F-50), large nanoflowers with 200 nm diameter (F-200), and small nanogravels with 50 nm diameter (G-50), the F-50 exhibit the highest photocatalytic performance. To demonstrate the effectiveness of the small nanoflowers, we prepared CuS films on a hydrophobic flexible substrate by coating the F-50 dispersion, indicating its potential for food packaging or antibacterial film applications. Finally, we demonstrated that the F-50 film can effectively eradicate gram-positive and -negative bacteria.

2. Experimental

2.1. Synthesis of CuS NPs, preparation of antibiotic film and characterization

Copper(II) acetate monohydrate (≥99.0 %), thiourea (≥99.0 %), and sodium dodecyl sulfate (SDS, ≥99.0 %) were purchased from Sigma-Aldrich. All chemicals were directly used without further purification. CuS NPs with various morphologies and particle sizes were synthesized via a chemical co-precipitation method by changing the synthesis temperature and thiourea addition rate. First, 0.4 g of SDS, as a surfactant, was dissolved in 20 mL of deionized (DI) water. Next, 0.198 g of copper acetate monohydrate and 0.152 g of thiourea were separately dissolved in 20 mL of DI water [30]. Thereafter, the copper acetate solution was slowly added to the SDS solution, and the mixture was slowly heated under continuous stirring for 1 h using a hotplate with an external temperature probe until the temperature reached 70, 80, or 90 °C. Subsequently, 20 mL of thiourea was added drop-wise to the solution with vigorous stirring, and its addition rate was adjusted to 0.01, 0.1, and 1.0 mL/s with a burette using a polytetrafluoroethylene (PTFE) plug. During this process, the solution color changes from sky blue to white. The solution was heated continuously with vigorous stirring for 24 h, and finally, a dark-green-colored dispersion was obtained. The products were washed several times with DI water and then freeze-dried to maintain the shape and size of the NPs.

To fabricate transparent flexible CuS films by coating F-50 dispersion onto a polyethylene terephthalate (PET) film, the dispersion medium was substituted from water to toluene using centrifugal separation. The dispersion was centrifuged and washed thrice with DI water, ethanol, and toluene. The dispersion was coated on the PET film (5 × 5 cm^2) by spin coating (30 s at 3000 rpm), followed by drying at 60 °C for 5 min. The coating and heating processes were repeated three times.

The structural characteristics of the synthesized CuS NPs were evaluated via X-ray diffraction (XRD, PANalytical, X'Pert Powder) with a Cu Kα radiation source. The morphology, lattice fringes and selected area electron diffraction (SAED) patterns of CuS NPs were observed using transmission electron microscopy (TEM: HT-7700, Hitachi), a high-resolution TEM (HR-TEM: Titan G2 80–200, FEI), and a field-emission scanning electron microscopy (FE-SEM: JSM-6701F, JEOL). The chemical states of CuS NPs were analyzed by X-ray photoelectron spectroscopy (XPS: Nexsa, Thermo Fisher Scientific) using a monochromatic Al Kα X-ray source (1486.6 eV) with a spot size of 400 μm. Binding energies were provided with respect to the C 1s peak of the hydrocarbons at 285.0 eV. The chemical composition was examined using energy dispersive X-ray spectroscopy (EDS: S-4800 equipped with a Horiba EX-250, HITACHI). The absorbance spectra of CuS NPs were measured by an ultraviolet–visible (UV–Vis) spectrometer (Carry 5000, Agilent).

2.2. Photocatalytic and antibacterial activity test

The photocatalytic activity was evaluated via Rhodamine B (RhB) dye degradation tests [31–34], under the irradiation of a light-emitting diode (LED) lamp-based solar simulator (Newport, LSH-7320, Class ABA) with a power density of 100 mW/cm^2. First, 4 mg of CuS powder was added to 20 mL RhB solution (25 mg/L). The solutions were maintained under dark conditions with stirring for 20 min to achieve an adsorption–desorption equilibrium. Subsequently, the solution was irradiated using an LED lamp for 1 h under continuous stirring. For analysis, 1 mL of solution was extracted from the system at 10 min intervals. The sampling solution was filtered using a 0.2 μL PTFE filter to eliminate residual CuS powder. The solution concentration was analyzed by observing the peak intensity at 554 nm using an UV–Vis spectrometer (Carry 5000, Agilent).

For the evaluation of the antibacterial ability of F-50, the most effective photocatalyst which will be shown later, the gram-negative *Escherichia coli* (*E. coli*; ATCC 8739) and the gram-positive *Staphylococcus aureus* (*S. aureus*; ATCC 6538) were used in this study. Each bacterial strain was sub-cultured overnight at 37 °C on nutrient agar (NA; 15.0 g/L agar, 5.0 g/L meat extract, 10.0 g/L peptone and 5.0 g/L sodium chloride) plates to obtain fresh cultures. Isolated colonies were taken using a sterile loop and suspended in 10 mL of 1/500 nutrient broth (NB; 3.0 g/L meat extract, 10.0 g/L peptone, and 5.0 g/L sodium chloride). Cell number was adjusted to approximately 1.5 × 10^8 cells/mL, corresponding to the McFarland 0.5 standard. These suspensions were diluted in sterile PBS 1 × , to get an inoculum with a final concentration ranging approximately 1.3 × 10^6 cells/mL (*S. aureus*) and 2.1 × 10^6 cells/mL (*E. coli*) for the strains. Bacterial counts were evaluated by determining the colony-forming units (CFUs)/mL after 10-fold dilutions in PBS 1 × and plating onto nutrient agar (NA; 15.0 g/L agar, 5.0 g/L meat extract, 10.0 g/L peptone and 5.0 g/L sodium chloride) plates followed by incubation at 37 °C overnight.

According to the ISO 22196:2011 standard [35], the antibacterial activity of F-50 coating films was determined by quantifying the recovery of bacteria held in contact for 24 h with these surfaces at 37 °C under a relative humidity of above 90 %, and the analysis was performed

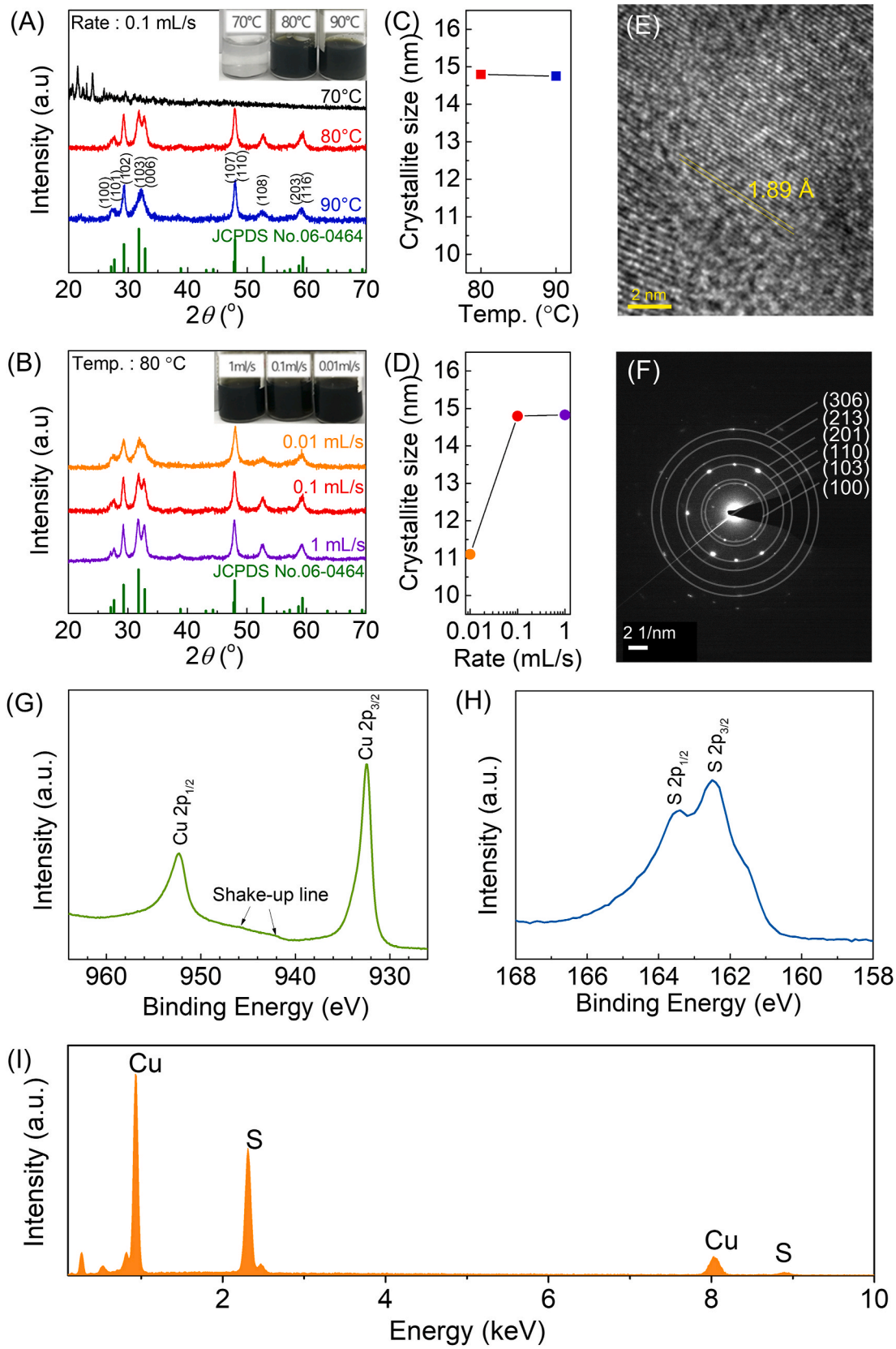

Fig. 1. Powder X-ray diffraction (XRD) patterns of the synthesized CuS nanoparticles (NPs) as a function of (A) synthesis temperature (thiourea addition rate: 0.1 mL/s) and (B) thiourea addition rate (temperature: 80 °C). Inset images show the corresponding CuS dispersion. Crystallite size calculated via XRD peak broadening depending on (C) synthesis temperature at a thiourea addition rate of 0.1 mL/s and (D) thiourea addition rate at a fixed temperature of 80 °C. (E) High-resolution transmission electron microscopy (HR-TEM) image and (F) the selected area electron diffraction (SAED) patterns of CuS NPs synthesized under the conditions of 80 °C and 0.01 mL/s. X-ray photoelectron spectroscopy (XPS) spectra of (G) Cu 2p and (H) S 2p, and (I) energy dispersive X-ray spectroscopy (EDS) spectra of CuS NPs synthesized under the conditions of 80 °C and 0.01 mL/s.

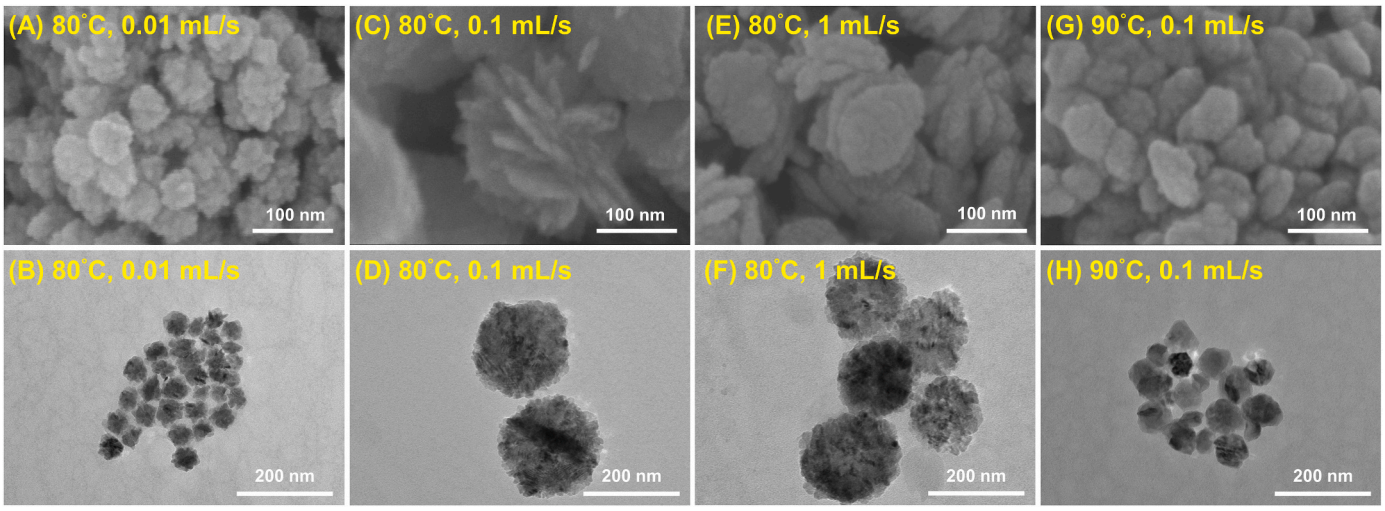

Fig. 2. Scanning electron microscopy (SEM) and transmission electron microscopy (TEM) images of CuS NPs synthesized under the conditions of (A, B) 80 °C and 0.01 mL/s, (C, D) 80 °C and 0.1 mL/s, (E, F) 80 °C and 1 mL/s, and (G, H) 90 °C and 0.1 mL/s.

in triplicate. The antibacterial test was conducted in the absence of the light. Briefly, F-50 coating films (5 × 5 cm^2) were placed into sterile petri dishes with the glazed surface uppermost. Then, an aliquot of 400 μL of the test inoculum was pipetted onto the surface of each sample and covered with a pre-sterilized polypropylene film (4 × 4 cm^2). After 24 h incubation, microorganisms were recovered from samples by adding 10 mL of soybean casein digest broth with lecithin and polyoxyethylene sorbitan mono-oleate (SCDLP; 17 g/L casein peptone, 3 g/L soy peptone, 5 g/L sodium chloride, 2.5 g/L dipotassium hydrogen phosphate, 2.5 g/L glucose, 1 g/L lecithin and 7 g/L tween 80) and shaking them for 5 min to achieve detachment of the bacteria from the surface. After this step, 10-fold serial dilutions in PBS 1 × were performed, and CFUs were counted on plate count agar (PCA) plate, following incubation at 37 °C for 24 h. As controls, untreated films were processed as previously described, immediately after bacteria deposition to represent the inoculum and after incubation for 24 h to evaluate antimicrobial activity.

3. Results and discussion

3.1. Structural and compositional characterization

X-ray powder diffraction analysis was conducted to study the crystal structure and crystallite size of the synthesized CuS NPs as a function of the synthesis temperature and thiourea addition rate (Fig. 1). Fig. 1A and B shows the XRD patterns of the CuS NPs depending on the synthesis temperature and thiourea addition rate, respectively. For the CuS NPs synthesized at 80 and 90 °C, peaks corresponding to the (100), (101), (102), (103), (006), (107), (110), (108), (203), and (116) diffraction planes are observed at 27.10°, 27.68°, 29.23°, 31.78°, 32.78°, 47.73° 47.89°, 52.67°, 58.66°, and 59.21°, respectively, confirming the successful synthesis of covellite CuS with a hexagonal structure (space group: $P6_3/mmc$) [36]. All peaks are well matched with those in JCPDS card no. 06–0464 without any secondary phase, such as Cu_xS, copper oxide, or copper hydroxide. However, the powder synthesized at 70 °C shows a distinct white color and no XRD peaks for the covellite CuS. (Fig. 1A). Because thiourea decomposes to sulfur at temperatures ≥80 °C, the white color indicates the presence of a copper–thiourea complex [30]. From Fig. 1B, all three powders synthesized at 80 °C show the same diffraction pattern regardless of the thiourea addition rate. Therefore, the temperature affects the formation of the hexagonal CuS phase, whereas the thiourea addition rate does not critically impact the CuS phase formation.

The crystallite size was calculated using the Debye–Scherrer formula (**eq. (1)**).

$$D = \frac{K\lambda}{\beta \cos\theta} \quad (1)$$

where D is the crystallite size of the particle; K is the shape factor (=0.9); λ is the X-ray wavelength (1.541 Å); β represents the full-width at half maximum; and θ is the peak position. The CuS NPs synthesized at 80 and 90 °C show nearly identical crystallite sizes of 14.8 and 14.7 nm, respectively (Fig. 1C). Similarly, as shown in Fig. 1D, the crystallite sizes of the CuS NPs synthesized with the addition rates of 0.1 and 1.0 mL/s are comparable (~15 nm). However, the CuS NPs synthesized with the lowest addition rate of 0.01 mL/s exhibited a substantially small crystalline size of ~11 nm. Therefore, although the thiourea addition rate has negligible effects on the CuS phase formation, it significantly influences the crystallite size, particularly at low addition rates.

The HR-TEM image of CuS NPs (Fig. 1E) displayed a lattice fringe spacing of 0.189 nm, corresponding to the interplanar spacing of (110) lattice planes of hexagonal CuS. The SAED pattern exhibited bright spots and rings with a high intensity. These results confirm that the CuS NPs are highly crystalline, consistent with the XRD analysis results (Fig. 1F).

We conducted XPS and EDS studies to identify the chemical composition of CuS NPs. In Fig. 1G, XPS peaks appear around 932.5 eV and 952.4 eV, corresponding to the binding energy of Cu $2p_{3/2}$ and Cu $2p_{1/2}$, respectively. These values align with the reported peaks for CuS [37,38]. A shake-up line is observed between the binding energies of Cu $2p_{3/2}$ and Cu $2p_{1/2}$ due to Cu(II) in the paramagnetic chemical state of Cu^{2+} [39]. The S 2p spectrum exhibits a characteristic doublet peak, indicative of metal sulfide [40,41]. Peaks at approximately 162.5 eV and 163.5 eV are attributed to S $2p_{3/2}$ and S $2p_{1/2}$, respectively [42] (Fig. 1H). EDS analysis revealed the presence of copper and sulfur, with a copper-to-sulfur atomic ratio 51.7 : 48.3, closely matching the intended composition.

3.2. Morphological properties

The size and morphology of CuS NPs synthesized under various conditions were evaluated via SEM and TEM analyses. Fig. 2A–F shows CuS NPs synthesized at 80 °C with distinct sizes depending on the thiourea addition rate. All samples obtained at 80 °C show similar flower-like morphology, regardless of the thiourea addition rate. Notably, the CuS NPs synthesized with an addition rate of 0.01 mL/s (named F-50) showed an average particle size of ~50 nm. In contrast, those synthesized with addition rates ≥0.1 mL/s showed comparable particle sizes of ~200 nm (named F-200). Significantly, when the

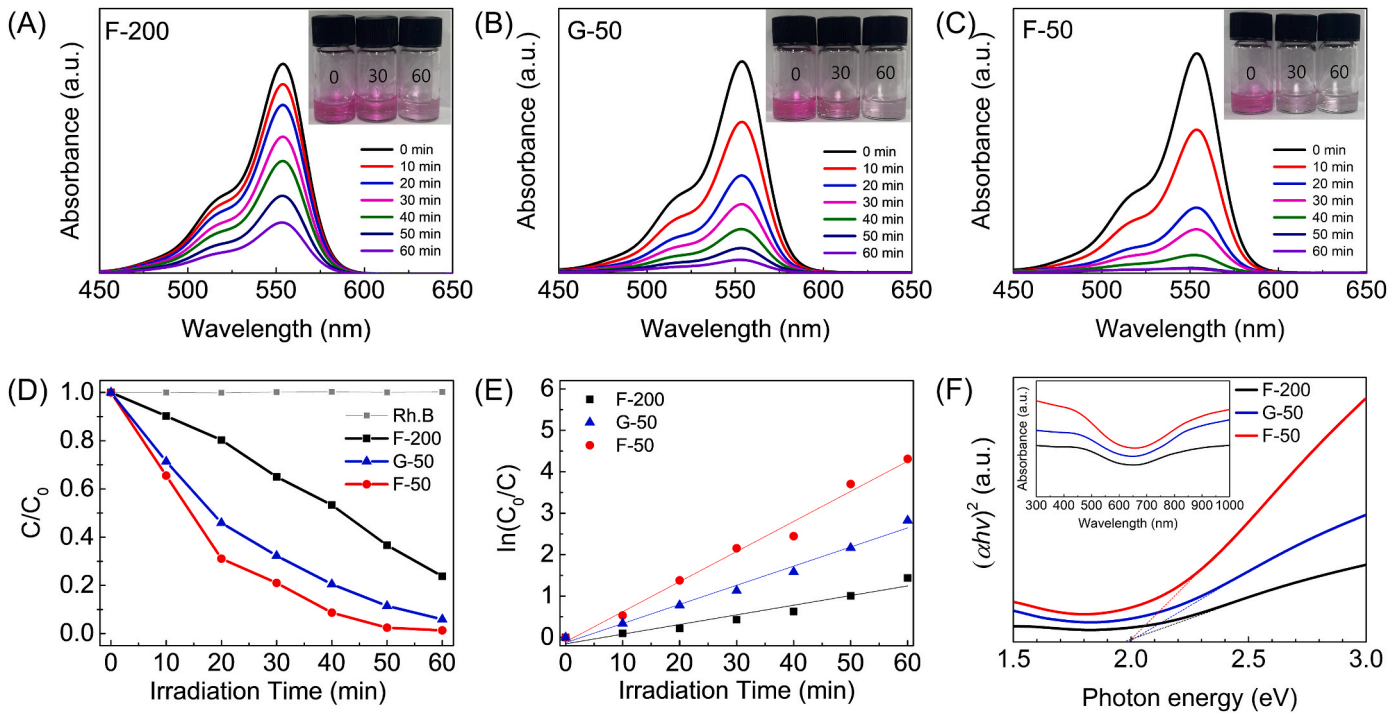

Fig. 3. Time-course UV–Vis absorbance spectra of the RhB dye during the photocatalytic test under LED irradiation. (A) F-200, (B) G-50, and (C) F-50. (D) Concentration variation of the RhB dye with the irradiation time. (E) Plot of $\ln(C_0/C)$ versus the irradiation time. Solid lines represent the fitting using a pseudo-first-order reaction rate of the corresponding samples. (F) Tauc-plot of F-200, G-50 and F-50. The inset shows UV–Vis absorption spectra.

synthesis temperature was increased to 90 °C (named G-50), the particle size reduced from 200 to ~50 nm (Fig. 2G and H). Furthermore, the morphology changed from nanoflower to nanogravel, i.e., the NPs synthesized at 90 °C exhibited a smoother surface (i.e., a lower surface roughness). Therefore, the synthesis temperature and thiourea addition rate significantly influence the microstructure, morphology, and particle size.

The dramatic change in morphology can be attributed to the release rate of sulfur ions (S^{2-}) resulting from the decompositions of thiourea and the local concentration of S^{2-} near the nucleation sites, which govern the nucleation and growth process of CuS NPs [22,25,43,44]. When thiourea solution is introduced into the copper acetate solution, it is well-known that the copper-thiourea complex is formed [22]. In cases where thiourea is supplied rapidly (i.e., at an addition rate of ≥0.1 mL/s), the local temperature near the complex remains below 80 °C for a while. Consequently, S^{2-} ions are gradually released due to the heat-induced decompositions of thiourea and gradually combines with Cu^{2+} ions to form CuS nuclei. It has been reported that CuS crystallites undergo preferentially oriented growth when S^{2-} is released slowly after nucleation, resulting in nanoplates [25,26]. The growth along the <110> direction is preferred while the growth along the <001> direction is suppressed, exposing the {001} plane [45,46]. As the reaction proceeds, heterogeneous nucleation and growth take place on the (001) plane to reduce the surface energy of the nanoplate, eventually forming hierarchical flower-shaped nanoparticles (F-200) [25]. On the other hand, when the reaction temperature is increased (e.g., to 90 °C), the local temperature may not decrease below the decomposition temperature of thiourea. As a result, S^{2-} ions are released rapidly, leading to immediate nucleation and fast growth, resulting in small, irregularly shaped gravel-like nanoparticles (G-50) with no or less preferred orientation [44]. In stark contrast, when thiourea is introduced at an extremely slow rate at 80 °C, the local temperature remains higher than the thiourea decomposition temperature. Consequently, the copper-thiourea complex releases S^{2-} ions and forms nuclei quickly. As the further sulfur supply requires a long time, nuclei concentration gradually increases until it reaches a critical level. Beyond this point, the added thiourea is more likely to be consumed for the growth of existing nuclei, rather than creating new nuclei. In this scenario, the growth of nanoflowers is constrained due to the high concentration of nuclei compared to the case of rapid sulfur source supply, leading to the formation of tiny, flower-like uniform NPs (F-50).

3.3. Photocatalytic properties

The photocatalytic performance of the three types of CuS NPs was investigated via RhB dye degradation experiments under LED illumination (100 mW/cm^2). The efficiency of the RhB degradation is compared using the time-dependent UV–Vis absorption spectra of the RhB solution. The absorption peak of RhB dye at 554 nm was used to quantify the concentration of the residual RhB dye. As shown in Fig. 3A–C, in all sample spectra, the intensity of the absorption peaks continuously decreases without any changes in their position during the photocatalytic reactions.

Fig. 3D and E shows the changes in the concentration of the RhB solution as a function of the irradiation time. The change in the concentration of the RhB solution in the absence of CuS NPs was also examined for comparison. The RhB solution without CuS NPs does not show any concentration changes, whereas the solution with CuS NPs shows a significant change in the concentration under LED irradiation. In this study, the most rapid decrease in the RhB dye concentration was observed for F-50, followed by G-50 and F-200. This result indicates that the smaller the NP size, the higher the photocatalytic activity. The photocatalytic degradation process was fitted using a pseudo-first-order kinetic model (**eq. (2)**):

$$\ln\left(\frac{C_0}{C_t}\right) = kt \tag{2}$$

where C_0 and C_t are the RhB concentrations at the initial state and at t time, respectively, and k is the rate constant (min^{-1}). The photodegradation rate constants of the F-200, F-50, and G-50 photocatalysts

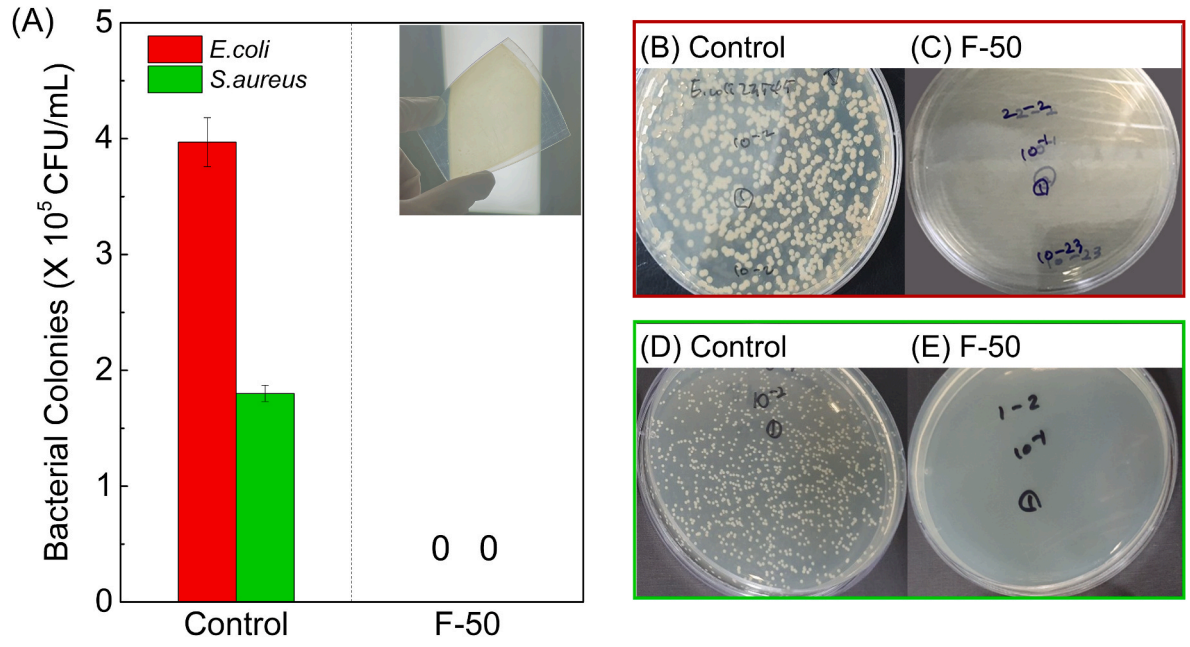

Fig. 4. (A) Bacterial colonies of untreated PET film (control) after 24 h and F-50 CuS NPs coating film after 24 h against *E. coli* (ATCC 8739) and *S. aureus* (ATCC 6538). Insert image display PET film coated by F-50, (B–C) Agar plates of *E. coli* in control and F-50 after 24 h, respectively, (D–E) Agar plates of *S. aureus* in control and F-50 after 24 h, respectively.

were calculated to be 0.0233, 0.0726, and 0.0462 min^{-1}, respectively. This result indicates that F-50 displays the highest degradation rate among the analyzed samples. When CuS NPs absorb the light, conduction band electrons (e^-) and valence band holes (h^+) are generated. These carriers migrate to the surface and engage the redox interaction with O_2 and H_2O adsorbed on the surface of photocatalyst, producing the ROS such as hydrogen peroxide (H_2O_2), hydroxyl radicals ($OH^•$), superoxide radicals ($O_2^{•-}$) and singlet oxygen ($^1O_2$) **(eqs. (3)–(6))** [47]. The generated ROS break down the Rh.B molecule into smaller non-toxic molecules, ultimately resulting in the formation of CO_2 and H_2O.

$$CuS + hv\ (\text{photon energy}) \rightarrow e^- + h^+ \left[hv \geq E_g\right] \quad (3)$$

$$O_2 + e^- \rightarrow O_2^{\cdot -} \quad (4)$$

$$H_2O + h^+ \rightarrow OH^{\cdot} + H^+ \quad (5)$$

$$O_2^{\cdot -} + H^+ \rightarrow H_2O^{\cdot} \quad (6)$$

$$2H_2O^{\cdot} \rightarrow H_2O_2 + O_2 \quad (7)$$

The optical properties of F-200, G-50 and F-50 were investigated to determine if their optical characteristics influence photocatalytic performance. Fig. 3F show the UV–Vis absorption spectra and the Tauc plot of CuS NPs. The bandgap of F-200, G-50 and F-50 are 1.98, 1.99 and 1.99 eV, respectively, which are consistent with the previous work [48]. While all spectra appear similar, F-50 sample exhibited the highest absorbance in the range of 300–620 nm. Notably, all spectra show the absorption in the near-infrared (NIR) region because of localized surface plasmon resonance (LSPR) characteristic of CuS NPs in the NIR region [49,50].

Based on analysis of the morphology and optical properties of CuS NPs, the superior photocatalytic performance of F-50 can be attributed to several factors. First, the flower-like morphology enhances light absorption due to multiple light scatterings [23,51], as observed in the absorption spectrum (Fig. 3F). In additions, the tiny size facilitates the migration of charge from the bulk to the surface [52]. Furthermore, its tiny flower-like structure contributes to a substantial specific surface area, hence providing abundant active sites for reactions [22].

Table 1
Summarization of previous reports on CuS-based antibacterial films coated on PET, Teflon, fiber and glass.

Sample type	Test time (hour)	Antibacterial activity (%)		Reference
		Gram negative bacteria	Gram positive bacteria	
Agar-CuS nanocomposite /Teflon film	9	>99.9	Non-effective	[61]
Alginate-CuS nanocomposite/ Teflon film	12	>99.9	Non-effective	[62]
CuS NPs /PAN fibers	24	92	97.5	[63]
CuS NPs /glass	24	>99.9	>99.9	[64]
CuS NPs /PET film	24	>99.9	>99.9	this work

3.4. Antibiotic properties

As previously mentioned, the antibiotic properties are closely linked to the ability of ROS generation because the generated ROS damage the vital cellular components such as lipids, proteins, and DNA, ultimately leading death of the pathogens [53]. CuS NPs are known for capability to eliminate pathogens by generating ROS through their photocatalytic [54,55], photothermal effect [56,57] and redox cycling of copper ions [58,59]. For photocatalytic and photothermal bacterial inactivation, the light irradiation is essential. However, the antibacterial properties through the redox cycling of copper ions can occur even in the absence of the light. Given that the ROS production reaction takes place on the surface of CuS NPs, it is highly likely that samples with high efficiency in generating ROS under light conditions, such as F-50, also possess the superior ability to generate ROS under dark conditions [8]. Therefore, we conducted antibacterial test with F-50, which exhibited the highest photocatalytic efficiency, against the Gram-negative *E. coli* (ATCC 8739)

and Gram-positive *S. aureus* (ATCC 6538) bacteria to demonstrate the its antibacterial features under dark conditions.

The antibacterial test was done by quantifying the bacterial recovery after 24 h of contact with F-50 films, following the ISO 22196:2011 standard [35]. Details of the experimental procedure can be found in the Experimental section. F-50 films were successfully prepared on flexible PET substrates using the F-50 dispersion that underwent medium exchange, as depicted in the insert image of Fig. 4. Initially, the average colony counts of *E. coli* and *S. aureus* on the samples were 6.7 and 6.1 $\times$ 10^4 CFU/mL, respectively. After 24 h of incubation, the average colony count of *E. coli* and *S. aureus* on the bare PET film without CuS (control) increased to 3.97 and 1.8 $\times$ 10^5 CFU/mL, respectively. In stark contrast, all bacteria on the F-50 film were eliminated, as shown in Fig. 4A, C, and E. Table 1 compares our results with previously reported results of antibacterial tests for CuS-based films coated on various substrates. This outcome underscores the potent antibacterial activity of CuS NPs against both gram-negative and gram-positive bacteria, even in the absence of light. The antibacterial activity of CuS NPs can be enhanced by light irradiation because of their photocatalytic and photothermal effect as reported in previous studies [8,54,60]. In additions, given its transparency and flexibility, our antibacterial film holds promise for diverse applications.

4. Conclusions

We successfully synthesized CuS NPs exhibiting nanoflower morphology, with particle sizes of 50 nm (F-50) via a cost-effective and scalable chemical co-precipitation method. The F-50 was obtained by controlling the synthesis temperature and thiourea addition rate without additional complex procedures and additives. All samples synthesized at 80 °C exhibited flower-like shapes regardless of the thiourea addition rate, while 90 °C led to gravel-like shapes. When the thiourea addition rate was reduced to 0.01 mL/s, a substantially smaller particle size (~50 nm) with flower shape was obtained. F-50 exhibited the highest photocatalytic activity for the degradation of the RhB dye solution. It was attributed enhanced light absorption, charge migration and high specific area due to the smallest NP size with the high surface roughness. The flexible transparent F-50 film on PET exhibited excellent antibiotic activity against both the Gram-negative *E. coli* (ATCC 8739) and Gram-positive *S. aureus* bacteria under dark conditions. We demonstrated the F-50 was effective in generating ROS under both light and dark conditions, highlighting its superior photocatalytic and antibacterial performance. Our results provide significant insights into controlling the morphology and particle size of CuS NPs without complex procedures and are expected to aid the diverse applications of CuS NPs.

Declaration of competing interest

The authors declare that they have no known competing financial interests or personal relationships that could have appeared to influence the work reported in this paper.

Acknowledgments

This work was supported by the National Research Foundation of Korea (NRF) funded by the Ministry of Science, ICT (No. 2019R1A2C1084010, and 2022M3J1A1085285).

References

[1] Tao Y, Ju E, Ren J, Qu X. Bifunctionalized mesoporous silica-supported gold nanoparticles: intrinsic oxidase and peroxidase catalytic activities for antibacterial applications. Adv Mater 2015;27:1097–104.
[2] Sharma VK, Yngard RA, Lin Y. Silver nanoparticles: green synthesis and their antimicrobial activities. Adv Colloid Interface Sci 2009;145:83–96.
[3] Malachová K, Praus P, Rybková Z, Kozák O. Antibacterial and antifungal activities of silver, copper and zinc montmorillonites. Appl Clay Sci 2011;53:642–5.
[4] Safdar M, Ozaslan M, Khailany RA, Latif S, Junejo Y, Saeed M, Al-Attar MS, Kanabe BO. Synthesis, characterization and applications of a novel platinum-based nanoparticles: catalytic, antibacterial and cytotoxic studies. J Inorg Organomet Polym Mater 2020;30:2430–9.
[5] Fang G, Li W, Shen X, Perez-Aguilar JM, Chong Y, Gao X, Chai Z, Chen C, Ge C, Zhou R. Differential Pd-nanocrystal facets demonstrate distinct antibacterial activity against Gram-positive and Gram-negative bacteria. Nat Commun 2018;9:129.
[6] Jayaseelan C, Rahuman AA, Kirthi AV, Marimuthu S, Santhoshkumar T, Bagavan A, Gaurav K, Karthik L, Rao KVB. Novel microbial route to synthesize ZnO nanoparticles using Aeromonas hydrophila and their activity against pathogenic bacteria and fungi. Spectrochim Acta Mol Biomol Spectrosc 2012;90:78–84.
[7] Foster HA, Ditta IB, Varghese S, Steele A. Photocatalytic disinfection using titanium dioxide: spectrum and mechanism of antimicrobial activity. Appl Microbiol Biotechnol 2011;90:1847–68.
[8] Mutalik C, Okoro G, Krisnawati DI, Jazidie A, Rahmawati EQ, Rahayu D, Hsu W-T, Kuo T-R. Copper sulfide with morphology-dependent photodynamic and photothermal antibacterial activities. J Colloid Interface Sci 2022;607:1825–35.
[9] Slavin YN, Asnis J, Häfeli UO, Bach H. Metal nanoparticles: understanding the mechanisms behind antibacterial activity. J Nanobiotechnol 2017;15:65.
[10] Dharsana US, Sai Varsha MKN, Khan Behlol AA, Veerappan A, Thiagarajan R. Sulfidation modulates the toxicity of biogenic copper nanoparticles. RSC Adv 2015;5:30248–59.
[11] Ayaz Ahmed KB, Anbazhagan V. Synthesis of copper sulfide nanoparticles and evaluation of in vitro antibacterial activity and in vivo therapeutic effect in bacteria-infected zebrafish. RSC Adv 2017;7:36644–52.
[12] Reidy B, Haase A, Luch A, Dawson KA, Lynch I. Mechanisms of silver nanoparticle release, transformation and toxicity: a critical review of current knowledge and recommendations for future studies and applications. Materials 2013:2295–350.
[13] Wang G, Zhang M, Lu L, Xu H, Xiao Z, Liu S, Gao S, Yu Z. One-pot synthesis of CuS nanoflower-decorated active carbon layer for high-performance asymmetric supercapacitors. ChemNanoMat 2018;4:964–71.
[14] Liu C, Friedman O, Li Y, Li S, Tian Y, Golan Y, Meng Y. Electric response of CuS nanoparticle lubricant additives: the effect of crystalline and amorphous octadecylamine surfactant capping layers. Langmuir 2019;35:15825–33.
[15] Liu Y, Qin D, Wang L, Cao Y. A facile solution route to CuS hexagonal nanoplatelets. Mater Chem Phys 2007;102:201–6.
[16] Zhao B, Shao G, Fan B, Zhao W, Xie Y, Zhang R. Synthesis of flower-like CuS hollow microspheres based on nanoflakes self-assembly and their microwave absorption properties. J Mater Chem A 2015;3:10345–52.
[17] Chen Z, Zhao M, Lv X, Zhou K, Jiang X, Ren X, Mei X. Fast ion transport through ultrathin shells of metal sulfide hollow nanocolloids used for high-performance energy storage. Sci Rep 2018;8:30.
[18] Hsu Y-K, Chen Y-C, Lin Y-G. Synthesis of copper sulfide nanowire arrays for high-performance supercapacitors. Electrochim Acta 2014;139:401–7.
[19] Anichini C, Czepa W, Aliprandi A, Consolaro VG, Ersen O, Ciesielski A, Samorì P. Synthesis and characterization of ultralong copper sulfide nanowires and their electrical properties. J Mater Chem C 2021;9:12133–40.
[20] Shen J, Zhang Y, Chen D, Li X, Chen Z, Cao S-a, Li T, Xu F. A hollow CuS nanocube cathode for rechargeable Mg batteries: effect of the structure on the performance. J Mater Chem A 2019;7:21410–20.
[21] Li P, Wang M, Jiang M, Lai W, Li J, Liu K, Li H, Hong C. Application of a CuS/Au heterostructure with peroxidase-like activity in immunosensors. New J Chem 2022;46:13963–70.
[22] Adhikari S, Sarkar D, Madras G. Hierarchical design of CuS architectures for visible light photocatalysis of 4-chlorophenol. ACS Omega 2017;2:4009–21.
[23] Zhang Y-Q, Zhang B-P, Ge Z-H, Zhu L-F, Li Y. Preparation by solvothermal synthesis, growth mechanism, and photocatalytic performance of CuS nanopowders. Eur J Inorg Chem 2014;2014:2368–75.
[24] Kushwah R, Singh A, Anshul A, Mishra D, Amritphale SS. Facile and controlled synthesis of copper sulfide nanostructures of varying morphology. J Mater Sci Mater Electron 2017;28:5597–602.
[25] Fu W, Liu M, Xue F, Wang X, Diao Z, Guo L. Facile polyol synthesis of CuS nanocrystals with a hierarchical nanoplate structure and their application for electrocatalysis and photocatalysis. RSC Adv 2016;6:80361–7.
[26] Liu X, Guo M, Wei C, Ji X, Zheng W. Purposely synthesis of hierarchical CuS nanoflowers composed of ultrathin nanoflakes with exposed (001) facets using a solvent-template ionic liquid and their application in supercapacitors. Mater Sci Eng, B 2021;273:115433.
[27] Yang Z, Zhang S, Zheng X, Fu Y, Zheng J. Controllable synthesis of copper sulfide for nonenzymatic hydrazine sensing. Sensor Actuator B Chem 2018;255:2643–51.
[28] Shi B, Liu W, Zhu K, Xie J. Synthesis of flower-like copper sulfides microspheres as electrode materials for sodium secondary batteries. Chem Phys Lett 2017;677:70–4.
[29] Cheng Z, Wang S, Si D, Geng B. Controlled synthesis of copper sulfide 3D nanoarchitectures through a facile hydrothermal route. J Alloys Compd 2010;492:L44–9.
[30] Dutta A, Dolui SK. Preparation of colloidal dispersion of CuS nanoparticles stabilized by SDS. Mater Chem Phys 2008;112:448–52.
[31] Cho I-S, Kim DW, Lee S, Kwak CH, Bae S-T, Noh JH, Yoon SH, Jung HS, Kim D-W, Hong KS. Synthesis of Cu2PO4OH hierarchical superstructures with photocatalytic activity in visible light. Adv Funct Mater 2008;18:2154–62.
[32] Cho I-S, Bae ST, Kim DH, Hong KS. Effects of crystal and electronic structures of ANb2O6 (A=Ca, Sr, Ba) metaniobate compounds on their photocatalytic H2 evolution from pure water. Int J Hydrogen Energy 2010;35:12954–60.

[33] Lee S, Cho I-S, Lee DK, Kim DW, Noh TH, Kwak CH, Park S, Hong KS, Lee J-K, Jung HS. Influence of nitrogen chemical states on photocatalytic activities of nitrogen-doped TiO2 nanoparticles under visible light. J Photochem Photobiol Chem 2010;213:129–35.
[34] Park S, Baek S, Kim D-W, Lee S. Oxygen-vacancy-modified brookite TiO2 nanorods as visible-light-responsive photocatalysts. Mater Lett 2018;232:146–9.
[[35]] ISO 22196. Measurement of antibacterial activity on plastics and other non-porous surfaces. 2011.
[36] Shamraiz U, Hussain RA, Badshah A. Fabrication and applications of copper sulfide (CuS) nanostructures. J Solid State Chem 2016;238:25–40.
[37] Chen Q, Wu S, Xin Y. Synthesis of Au–CuS–TiO2 nanobelts photocatalyst for efficient photocatalytic degradation of antibiotic oxytetracycline. Chem Eng J 2016;302:377–87.
[38] Gan M, Lai S, Jiang S, Sun C, Song S. Dynamical transfer behavior and in situ interaction with H2O molecules of charge carriers over heterojunction in non-adiabatic systems. Appl Catal B Environ 2023;340:123278.
[39] Ghijsen J, Tjeng LH, van Elp J, Eskes H, Westerink J, Sawatzky GA, Czyzyk MT. Electronic structure of ${\mathrm{Cu}}_{2}$O and CuO. Phys Rev B 1988;38:11322–30.
[40] Zhang W, Xing P, Zhang J, Chen L, Yang J, Hu X, Zhao L, Wu Y, He Y. Facile preparation of novel nickel sulfide modified KNbO3 heterojunction composite and its enhanced performance in photocatalytic nitrogen fixation. J Colloid Interface Sci 2021;590:548–60.
[41] Song C, Wang X, Zhang J, Chen X, Li C. Enhanced performance of direct Z-scheme CuS-WO3 system towards photocatalytic decomposition of organic pollutants under visible light. Appl Surf Sci 2017;425:788–95.
[42] Wang Z, Rafai S, Qiao C, Jia J, Zhu Y, Ma X, Cao C. Microwave-assisted synthesis of CuS hierarchical nanosheets as the cathode material for high-capacity rechargeable magnesium batteries. ACS Appl Mater Interfaces 2019;11:7046–54.
[43] Tanveer M, Cao C, Ali Z, Aslam I, Idrees F, Khan WS, But FK, Tahir M, Mahmood N. Template free synthesis of CuS nanosheet-based hierarchical microspheres: an efficient natural light driven photocatalyst. CrystEngComm 2014;16:5290–300.
[44] Yadav S, Shrivas K, Bajpai PK. Role of precursors in controlling the size, shape and morphology in the synthesis of copper sulfide nanoparticles and their application for fluorescence detection. J Alloys Compd 2019;772:579–92.
[45] Yang Z, Li H, Feng S, Li P, Liao C, Liu X, Zhao J, Yang J, Lee P-H, Shih K. Multiform sulfur adsorption centers and copper-terminated active sites of nano-CuS for efficient elemental mercury capture from coal combustion flue gas. Langmuir 2018;34:8739–49.
[46] Morales-García Á, He J, Soares AL, Duarte HA. Surfaces and morphologies of covellite (CuS) nanoparticles by means of ab initio atomistic thermodynamics. CrystEngComm 2017;19:3078–84.
[47] Garcia-Segura S, Brillas E. Applied photoelectrocatalysis on the degradation of organic pollutants in wastewaters. J Photochem Photobiol C Photochem Rev 2017;31:1–35.
[48] Zheng L, Teng F, Ye X, Zheng H, Fang X. Photo/electrochemical applications of metal sulfide/TiO2 heterostructures. Adv Energy Mater 2020;10:1902355.
[49] Luther JM, Jain PK, Ewers T, Alivisatos AP. Localized surface plasmon resonances arising from free carriers in doped quantum dots. Nat Mater 2011;10:361–6.
[50] Zhao Y, Pan H, Lou Y, Qiu X, Zhu J, Burda C. Plasmonic Cu2−xS nanocrystals: optical and structural properties of copper-deficient copper(I) sulfides. J Am Chem Soc 2009;131:4253–61.
[51] Tian Q, Tang M, Sun Y, Zou R, Chen Z, Zhu M, Yang S, Wang J, Wang J, Hu J. Hydrophilic flower-like CuS superstructures as an efficient 980 nm laser-driven photothermal agent for ablation of cancer cells. Adv Mater 2011;23:3542–7.
[52] Sudrajat H, Babel S, Sakai H, Takizawa S. Rapid enhanced photocatalytic degradation of dyes using novel N-doped ZrO2. J Environ Manag 2016;165:224–34.
[53] Nosaka Y, Nosaka AY. Generation and detection of reactive oxygen species in photocatalysis. Chem Rev 2017;117:11302–36.
[54] Ma H, Wang K, Zeng Q, Li P, Lyu S, Li B, Luo X, Jiang L, Cao M, Liao B, Qiu Z, Hao L, Wang C. Photocatalytic properties and antibacterial mechanisms of microbial-derived ZnS/CuS nanocomposites. J Environ Chem Eng 2023;11:111425.
[55] Lv R, Liang Y-Q, Li Z-Y, Zhu S-L, Cui Z-D, Wu S-L. Flower-like CuS/graphene oxide with photothermal and enhanced photocatalytic effect for rapid bacteria-killing using visible light. Rare Met 2022;41:639–49.
[56] Xu G, Du X, Wang W, Qu Y, Liu X, Zhao M, Li W, Li Y-Q. Plasmonic nanozymes: leveraging localized surface plasmon resonance to boost the enzyme-mimicking activity of nanomaterials. Small 2022;18:2204131.
[57] Zhang X, Zhang G, Zhang H, Liu X, Shi J, Shi H, Yao X, Chu PK, Zhang X. A bifunctional hydrogel incorporated with CuS@MoS2 microspheres for disinfection and improved wound healing. Chem Eng J 2020;382:122849.
[58] Vincent M, Duval RE, Hartemann P, Engels-Deutsch M. Contact killing and antimicrobial properties of copper. J Appl Microbiol 2018;124:1032–46.
[59] Chen J, Pan H, Chen Y, Zhou Z, Jing G, Zhao X. Efficient activation of peracetic acid for abatement of tetracycline by W-doped CuS via regulating copper redox cycling. Chem Eng J 2023;464:142693.
[60] Li M, Liu X, Tan L, Cui Z, Yang X, Li Z, Zheng Y, Yeung KWK, Chu PK, Wu S. Noninvasive rapid bacteria-killing and acceleration of wound healing through photothermal/photodynamic/copper ion synergistic action of a hybrid hydrogel. Biomater Sci 2018;6:2110–21.
[61] Roy S, Rhim J-W, Jaiswal L. Bioactive agar-based functional composite film incorporated with copper sulfide nanoparticles. Food Hydrocolloids 2019;93:156–66.
[62] Roy S, Rhim J-W. Effect of CuS reinforcement on the mechanical, water vapor barrier, UV-light barrier, and antibacterial properties of alginate-based composite films. Int J Biol Macromol 2020;164:37–44.
[63] Wang Y, Wang W, Liu B, Yu D. Preparation of durable antibacterial and electrically conductive polyacrylonitrile fibers by copper sulfide coating. J Appl Polym Sci 2017;134:45496.
[64] Gargioni C, Borzenkov M, D'Alfonso L, Sperandeo P, Polissi A, Cucca L, Dacarro G, Grisoli P, Pallavicini P, D'Agostino A, Taglietti A. Self-assembled monolayers of copper sulfide nanoparticles on glass as antibacterial coatings. Nanomaterials 2020;10:352.